ELSEVIER

Contents lists available at ScienceDirect

Acta Materialia

journal homepage: www.elsevier.com/locate/actamat



The influence of helium and heavy ion irradiations on radiation responses of single crystal Cu with nanovoids: An in situ TEM study



Cuncai Fan^{a,*}, Zhongxia Shang^a, Meimei Li^b, Haiyan Wang^{a,c}, Anter El-Azab^{a,d}, Xinghang Zhang^{a,*}

- ^a School of Materials Engineering, Purdue University, West Lafayette, IN, 47907, USA
- ^b Nuclear Engineering Division, Argonne National Laboratory, Argonne, IL, 60439, USA
- ^c School of Electrical and Computer Engineering, West Lafayette, IN, 47907, USA
- ^d School of Nuclear Engineering, Purdue University, West Lafayette, IN, 47907, USA

ARTICLE INFO

Article history: Received 11 June 2022 Accepted 20 August 2022 Available online 21 August 2022

Keywords: In situ TEM Heavy ion irradiation Helium effect Void shrinkage Critical Bubble Model

ABSTRACT

Helium is a common nuclear reaction product, and it plays an important role in radiation-induced void swelling. Although extensive studies have been conducted to investigate the helium effects in metals and alloys, most of them were based on the post-irradiation analyses or computer simulations. Conclusive evidence that can demonstrate how voids evolve in the presence of He under high-temperature radiation remains limited. In this work, we performed *in situ* heavy ion radiation studies in a transmission electron microscope to compare the radiation response of the preexisting nanovoids in single crystal copper subjected to a single beam of 1 MeV Kr ions and a sequential dual beam of 14 keV He ion and 1 MeV Kr ion at 350 °C. Our studies revealed that the nanovoids would contract continuously until being eliminated when irradiated by a single beam of Kr ions. In comparison, the nanovoids in helium-injected Cu could reach a stable state and eventually stopped shrinking. Moreover, the influence of helium on the kinetics of void/bubble evolution under heavy ion irradiation was discussed within the framework of a proposed critical bubble model and bubble coarsening model.

© 2022 Acta Materialia Inc. Published by Elsevier Ltd. All rights reserved.

1. Introduction

The problem of void evolution under irradiation environment has been of great interest as void swelling has been widely observed in irradiated nuclear materials [1]. The nucleation and growth of voids are heavily influenced by various parameters, such as impurity and gases [2]. As a common nuclear reaction product arising from α decay or Deuterium-Tritium (DT) fusion, Helium (He) is the most important impurity that is inevitably present in the structural materials for fission reactors or in the plasma-facing materials for future fusion reactors [3,4]. To simulate its effects on void swelling from fission or fusion neutrons, multi-ion-beam technique has been proposed with He injected before or during energetic heavy ion irradiation [5,6]. The injected He is barely soluble in solids, and it tends to diffuse rapidly through the crystal lattice and combines with excess vacancies to precipitate as He bubbles [7,8]. Note that the bubbles are very different from voids. In general, the former ones refer to pressurized cavities usually

E-mail addresses: cuncaifan@gmail.com (C. Fan), xzhang98@purdue.edu (X. Zhang).

with a small size (<5 nm) and a spherical shape, while the latter ones are defined as large cavities under low-pressure or vacuum that exhibit facets along the close packed planes of the host lattice [9]. Whether a bubble can convert to a void is determined by irradiation conditions and the material's microstructures [10,11]. According to previous studies, the addition of He can have opposite effects on void swelling [12–16]. To understand the different behaviors of bubbles and voids under high-temperature irradiation environment, more in-depth investigations are required. In addition, most of the previous studies are based on post-irradiation analyses [17–22], and there are few studies on the kinetics of void evolution during ion irradiation process.

In situ transmission electron microscopy (TEM) ion irradiation experiment provides a unique opportunity for real-time observation of damage evolution in irradiated materials [23–25]. This technique enjoys the advantages of well-controlled experimental conditions and high-dose radiation damage in a short time [26], and it has been applied to refine classical theories and validate computer simulations [27,28]. However, the in situ studies that can demonstrate how He impacts void evolution (growth or shrinkage) during an irradiation process remain limited because of experimental difficulties. Although a couple of in situ TEM studies were

^{*} Corresponding authors.

reported on the irradiation-induced cavities [29-32], they have primarily focused on the bubble nucleation process or the interactions between bubbles and internal defects, such as dislocations [29] and grain boundaries [30]. It must be noted that the void embryos are so tiny in the early stage of their nucleation that they cannot be well imaged via a defocus or overfocus imaging condition [33]. Also, considering the free surface effect of TEM foils, it is difficult to examine void growth and swelling [34]. Recently, some in situ Kr ion irradiation studies have been performed in Cu with deliberately introduced nanovoids prior to irradiation [35,36]. Using this method, we have successfully obtained the kinetics of irradiation-induced void spheroidization, shrinkage and migration in single-crystal Cu with preexisting nanovoids [37,38]. The main objective for the current work is to explore the He effects on the nucleation and growth (or shrinkage) of voids under in situ heavy ion irradiation environment near the peak swelling temperature, 350 °C for Cu [39]. Moreover, the fluence of pre-injected He is as high as 2600 appm, which is significant and relevant for understanding the void swelling in fusion materials [3].

2. Experimental

Highly-textured Cu (110) films, \sim 2 μ m thick, were deposited on Si (112) substrates using direct current magnetron sputtering technique at room temperature. More detailed information regarding the sputtering deposition can be found elsewhere [37]. Planeview TEM specimens were fabricated from as-deposited Cu films via polishing, dimpling, and low-energy (3.5 keV) Ar ion milling.

In situ TEM irradiation experiments were conducted in the Intermediate Voltage Electron Microscope (IVEM) at Argonne National Laboratory (IL, USA). The IVEM consists of an ion accelerator attached to a Hitachi-9000 TEM microscope with ion beam incident at $\sim 30^{\circ}$ to the electron beam. Before irradiation, all TEM specimens were ramped up to a final temperature of 350 °C and annealed at the maximum temperature for \sim 0.5 h. Two sets of independent heavy ion irradiation experiments were performed using a single beam of 1 MeV Kr⁺⁺, and a dual beam of 14 keV He⁺ and 1 MeV Kr++. For single-beam irradiation, the specimen was directly irradiated by 1 MeV Kr $^{++}$ to a fluence of 2.0 \times 10¹⁴ ions cm⁻² with a flux of \sim 9.4 \times 10¹⁰ ions cm⁻²s⁻¹; for dual-beam irradiation, the specimen was first injected by 14 keV He⁺ to a fluence of 3.1 \times 10¹⁵ ions cm⁻² with a flux of \sim 6.25 \times 10¹¹ ions cm⁻²s⁻¹, then followed by the irradiation of 1 MeV Kr⁺⁺ with the same ion fluence/flux as those in single-beam case. Both single- and dualbeam irradiations were conducted at 350 °C. During irradiation, the microstructural evolutions were characterized by the Hitachi-9000 TEM operated at 200 kV, and a series of TEM micrographs were taken at certain doses and He concentrations when the ion beams were stopped. After irradiation, the specimens were reexamined at room temperature by an FEI Talos 200X TEM microscope also operated at 200 kV. The radiation dose (in dpa) and injected He concentration (in at. %) were calculated by Stopping and Range of Ions in Matter (SRIM) with Kinch-Pease method [40].

3. Results

Fig. 1(a) and (b) are the bright-field TEM micrographs, recorded along Cu [110], of plane-view specimens showing the representative faceted nanovoids with dark and white Fresnel fringes, respectively at under-focus ($\Delta f = -1.5 \ \mu m$) and over-focus ($\Delta f = +1.5 \ \mu m$) imaging conditions. Before *in situ* irradiation, the annealed sample at 350 °C for 0.5 h still contained faceted nanovoids, as demonstrated by Fig. 1(c). The TEM foil thickness was measured by convergent beam electron diffraction (CBED) technique [41]. Fig. 1(d) is the parallel K-M fringes for the area of irradiation, taken

under two-beam conditions with $(31\overline{1})$ strongly excited. The corresponding foil thickness λ was estimated as \sim 115 nm based on the plot of $(s_i/n_k)^2$ versus $(1/n_k)^2$ in Fig. 1(e). The SRIM calculated depth profiles of ion concentration and dose in Fig. 1(f) and (g) suggest that the majority of 1 MeV Kr⁺⁺ transmitted through the TEM foil and produced 1.0 dpa damage, while most of the 14 keV He⁺ remained inside the foil and amounted to 0.26 at. % He (2600 appm).

3.1. In situ 14 keV He⁺ injection

Fig. 2 shows the formation of He bubbles during the injection of 14 keV He+ into a TEM specimen at 350 °C. Initially in Fig. 2(a), there are some preexisting nanovoids introduced by film deposition. By a fluence of 1×10^{15} ions/cm² in Fig. 2(b), small bubbles started emerging from the matrix. The bubbles reached a maximum diameter (\sim 2 nm) by 2 \times 10¹⁵ ions/cm² as shown in Fig. 2(c). In the meantime, the bubble density kept increasing gradually. At the end of He injection in Fig. 2(d), the bubble density was around 1.8 \times 10²² /m³. It should be emphasized that the preexisting nanovoids gradually became gas-filled and pressurized with increasing He fluence, seemingly identical to the He bubbles in nature. However, for simplicity and discussion, we still differentiate preexisting voids from bubbles according to their creation history and the difference in morphology. In the following sections. voids only refer to the preexisting large cavities before irradiation, while bubbles refer to the tiny cavities nucleated from the matrix during dual-beam irradiation. As what we will present later, the voids and bubbles behave in quite different ways under the same heavy ion irradiation environment, although they both have a mixture of vacancies and He atoms.

3.2. In situ 1 MeV Kr⁺⁺ irradiation

According to our previous in situ study [37], the faceted voids in Cu tend to become spherical when irradiated by 1 MeV Kr++ at 350 °C, and the spheroidization process is able to complete at a rather low dose, ~0.15 dpa. For a spherical void, therefore, its size can be well characterized by its diameter. Moreover, in situ TEM experiment permits continuous observations on specific voids to investigate their size evolution. The void evolution between dualbeam (preinjected with He) irradiation and single-beam irradiation is compared in Fig. 3. Sequential TEM snapshots were taken over 0.25 to 1.00 dpa when all the irradiated voids are spherical. As shown in Fig. 3 (a)-(d), the single-beam irradiated voids exhibit a wide variety of shrinkage behaviors. It seems that most of them shrank rapidly and eventually disappeared at a certain dose, but some of them could survive the Kr++ irradiation to 1.00 dpa. For instance, 6 typical survivals labelled by A-F are all present in Fig. 3(a)-(d). In particular, the void A has an initial diameter that is slightly smaller than another two voids G and H, as demonstrated in Fig. 3(a). However, with increasing dose, the larger voids G and H shrank in a much faster way and totally disappeared at 1.00 dpa in Fig. 3(d), while the void A barely reduced in size. Such variations in shrinkage behavior might be associated with the different void positions inside TEM foil, which will be discussed later in detail.

Fig. 3(e-h) are the sequential TEM snapshots for the void evolution with preinjected He before Kr^{++} irradiation (see Section 3.1). It has been found that abundant bubbles rapidly nucleated homogeneously from the matrix, and they soon became saturated throughout the sample upon Kr^{++} irradiation. By 0.25 dpa in Fig. 3(e), the bubble density jumped to $1.47 \times 10^{23} \text{ m}^{-3}$. After that, however, the bubbles remained stable with little changes in size and density, albeit ongoing Kr^{++} irradiation, as demonstrated in Fig. 3(e-h). The preexisting voids, on the other hand, behaved

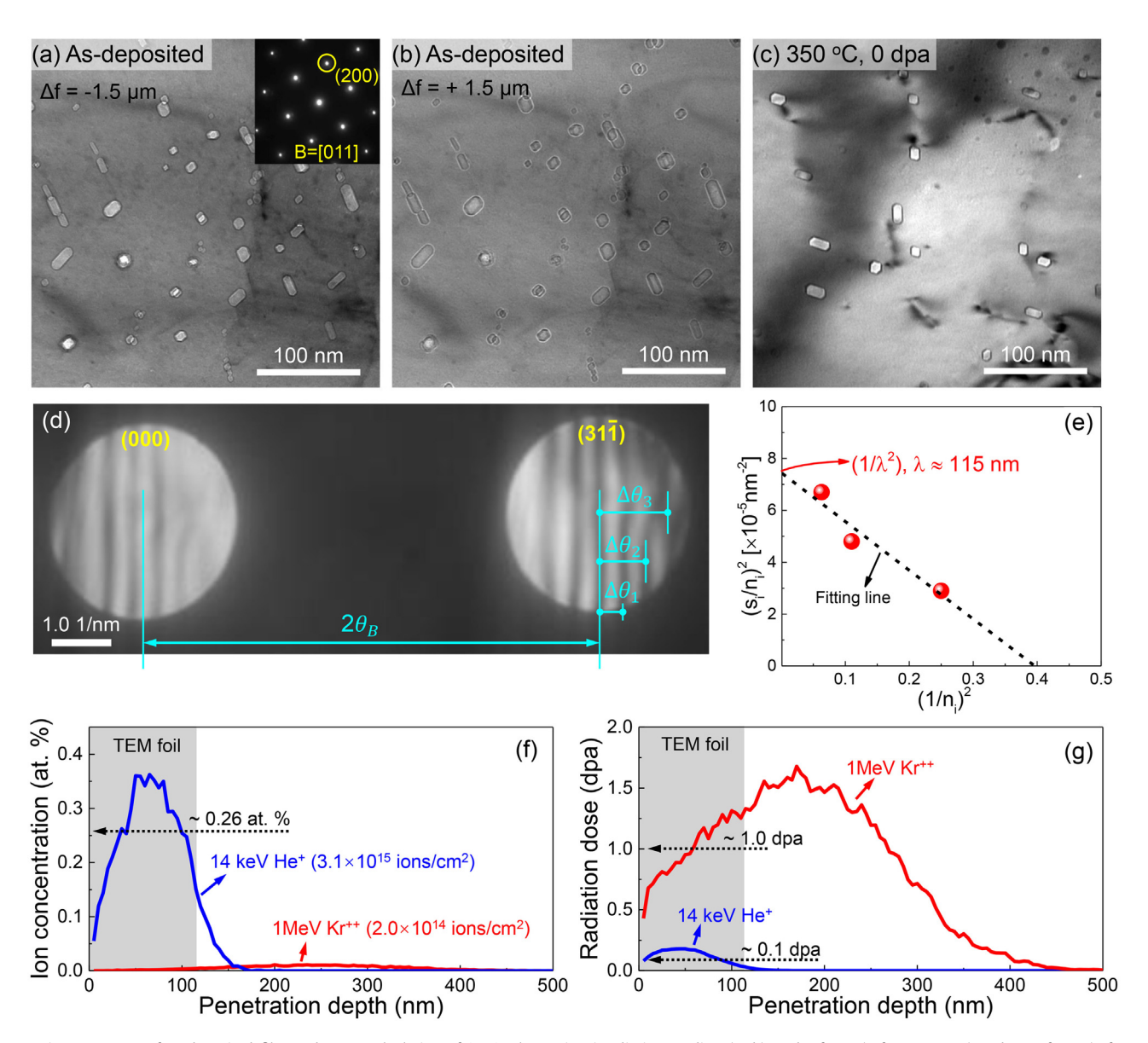


Fig. 1. Microstructures of as-deposited film and SRIM calculation of in situ heavy ion irradiation studies. (a, b) Under-focus ($\Delta f = -1.5 \ \mu m$) and over-focus ($\Delta f = +1.5 \ \mu m$) plane-view TEM micrographs of as-deposited single crystal (110) Cu film, with dark and white Fresnel fringes surrounding faceted nanovoids. The inserted SAD pattern shows single crystal-like diffraction along the Cu <011> zone axis. (c) Preexisting faceted nanovoids annealed at 350 °C for ~0.5 h before irradiation (0 dpa). (d) Parallel K-M fringes in a convergent-beam diffraction pattern taken under two-beam conditions with (31 $\overline{1}$) strongly excited. (e) Plot of $(s_i/n_k)^2$ against $(1/n_k)^2$. The TEM foil thickness is extrapolated to be 115 nm from the intercept $1/\lambda^2$. (f, g) Depth profiles of ion concentration and radiation dose along ion penetration depth calculated by SRIM.

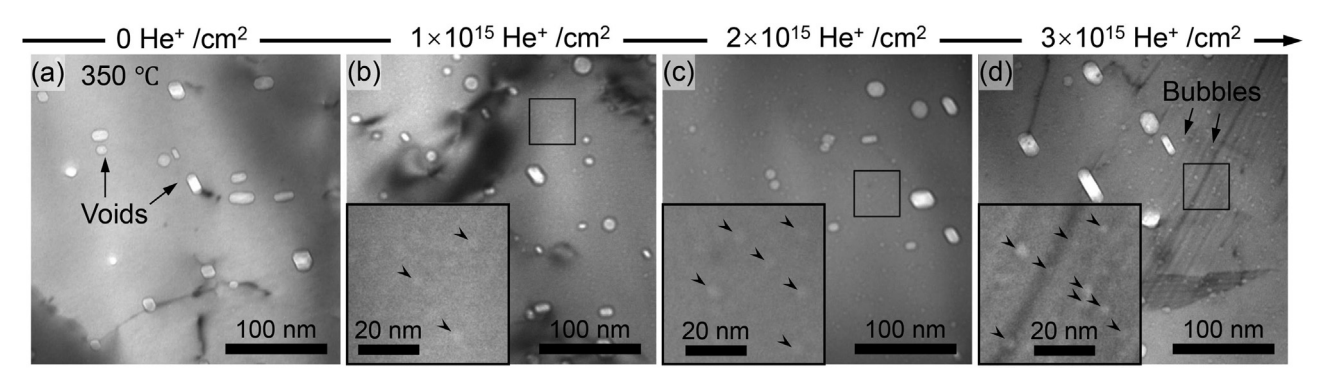


Fig. 2. In situ TEM snapshots showing the formation of bubbles during He injection at 350 °C. The enlarged views in (b-d) demonstrate the nucleation and growth of small bubbles (marked by arrows).

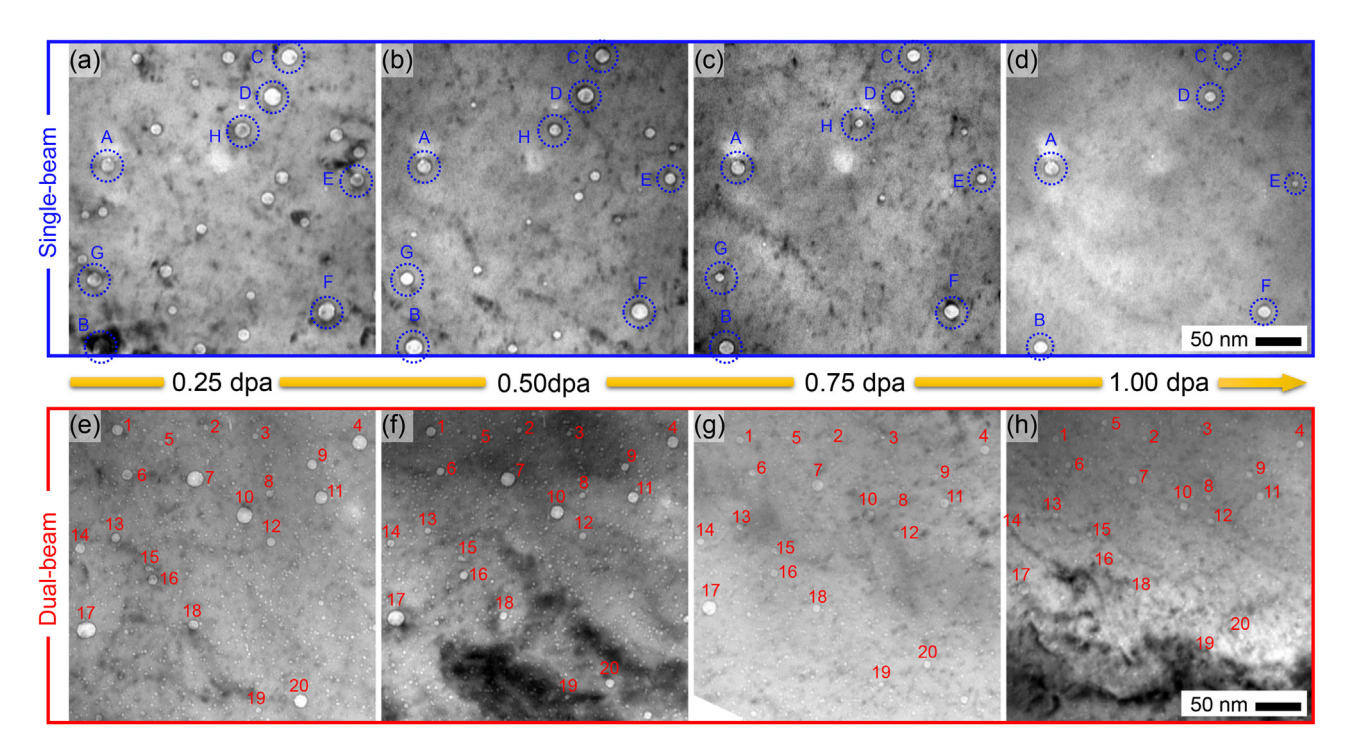


Fig. 3. Sequential TEM snapshots comparing the void shrinkage between (a-d) single-beam (1 MeV Kr^{++}) and (e-h) dual-beam (14 keV He^+ followed by 1 MeV Kr^{++}) irradiations over 0.25 to 1.00 dpa at 350 °C. (a-d) Most of the voids irradiated by single 1 MeV Kr^{++} shrank continuously, but their shrinkage rates varied. A-F mark the voids with a lower shrinkage rate that survived the irradiation to 1dpa; H and G mark the voids with a higher shrinkage rate that eventually vanished during the Kr^{++} irradiation. (e-h) In the presence of He, the irradiated voids first shrank gradually but then stopped shrinking when their size reduced to several nanometers. Representative voids are indicated by the numbers 1-20.

differently. In general, the larger voids first shrank, but in a later stage they stopped shrinking even when Kr++ irradiation continued. Some voids were carefully tracked as labelled by the numbers 1-20 in Fig. 3(e)-(h). Note that voids19 and 20 were obviously changing their positions with respect to the others. More detailed analyses on the void position change can be found in Supplementary Fig. S1 and S2. Considering the irradiated sample had fragmented into pieces after unloading from the IVEM column, we assume that the relative position changes for some voids, (e.g., voids19 and 20), might be caused by sample tilting when cracks were propagating at local regions. However, a careful inspection of Supplementary Fig. S2, the superimposed maps of all the voids at different doses, reveals that the small void 15 was clearly moving relative to the other voids around. As demonstrated in Fig. 4 (a), void 15 is only 7.6 nm in diameter, smaller than its neighboring voids 13, 14 and 16, and it is very close to void 16. With increasing dose, however, void 15 was obviously moving away from void 16, and their distance was increasing several times from 13 to 28 nm at 1.00 dpa as shown in Fig. 4 (d). The Kr ion irradiation-induced void (without He) migration has been reported in our recent in situ TEM irradiation study [37]. Moreover, it has been reported that small gas bubbles can migrate and coalesce into large ones when receiving sufficient thermal activation energies [42,43]. This statement is also consistent with our current in situ observations, and the evidence of bubble migration and coalescence is demonstrated in Fig. 4(c-d). As shown in Fig. 4(a-b), in addition to the large voids 13-16, there are a number of small bubbles randomly distributed in the observed area. With increasing dose, the small bubbles experienced a spatial redistribution, indicative of their migrations. By 0.75 dpa in Fig. 4(c), a large bubble (\sim 5.6 nm in diameter) was present in the yellow circle, presumably resulting from the bubble migration and coalescence. The new-born large bubble remained stable thereafter without any growth in size, as demonstrated in Fig. 4(d).

3.3. Bubble evolution

Fig. 5 shows the evolutions of bubble diameter D_B and density ρ_B for dual-beam irradiation. The entire process can be divided into two major parts, namely He+ injection and Kr++ irradiation, which can be further subdivided into 6 separate stages depending on the variations of D_B and ρ_B . Among different stages, Stage 1 refers to the incubation period when no bubbles could be detected by TEM, and it is followed by Stage 2 when bubbles started to nucleate and grow with increasing D_B/ρ_B . In Stage 3, D_B reached a maximum value (\sim 2.5 nm), while ρ_{B} kept increasing with increasing He fluence. After He $^+$ injection, ho_B was still relatively low, but it jumped dramatically when Kr++ irradiation occurred in the beginning of Stage 4. Beyond 0.25 dpa in Stage 5, the bubbles became saturated throughout the sample with little changes of ρ_B and D_B . In Stage 6, the bubbles were subject to coarsening with slight increase in average size and decrease in density. It is worth pointing out that some He-vacancy clusters might have formed during He⁺ injection, but they are too tiny to be detected by TEM. These clusters would further combine with excess vacancies and finally evolve into bubbles. This assumption accounts well for a dramatic density increase (from 1.8 \times 10^{22} $/m^3$ to 1.47 \times 10^{23} $/m^3)$ upon Kr⁺⁺ irradiation in Stage 4. The underlying mechanism of bubble evolution will be discussed later. At this point, we simply regard bubbles as a mixture of He atoms and vacancies, based on which two important conclusions can be drawn: (1) during He⁺ injection, bubble nucleation and growth are limited by low dose (0.1 dpa), in other words, scanty vacancies; (2) during Kr++ irradiation, bubble growth might be limited by a shortage of He atoms.

3.4. Void evolution

The variations of void radius R for single- and dual-beam irradiations are shown in Fig. 6(a). With increasing time (or dose), it

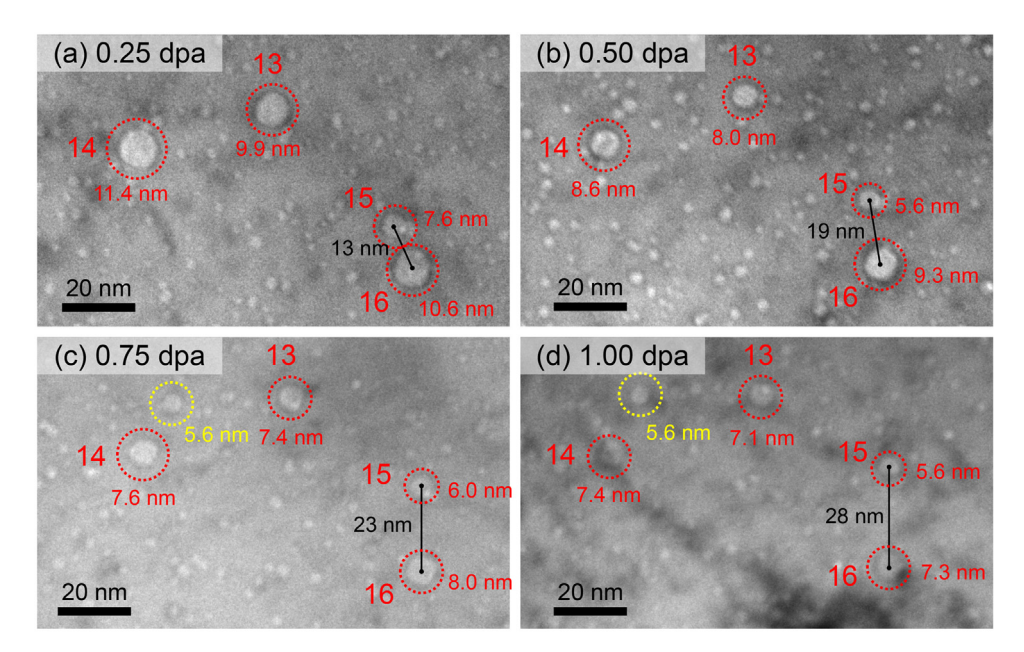


Fig. 4. A sequence of enlarged TEM snapshots at the same location containing the voids 13-16 labelled in Fig. 3 (e-h), showing the migration of void 15 and the formation of a large bubble between voids 13 and 14. The newly-formed bubble is marked by the yellow circle in (c) and (d).

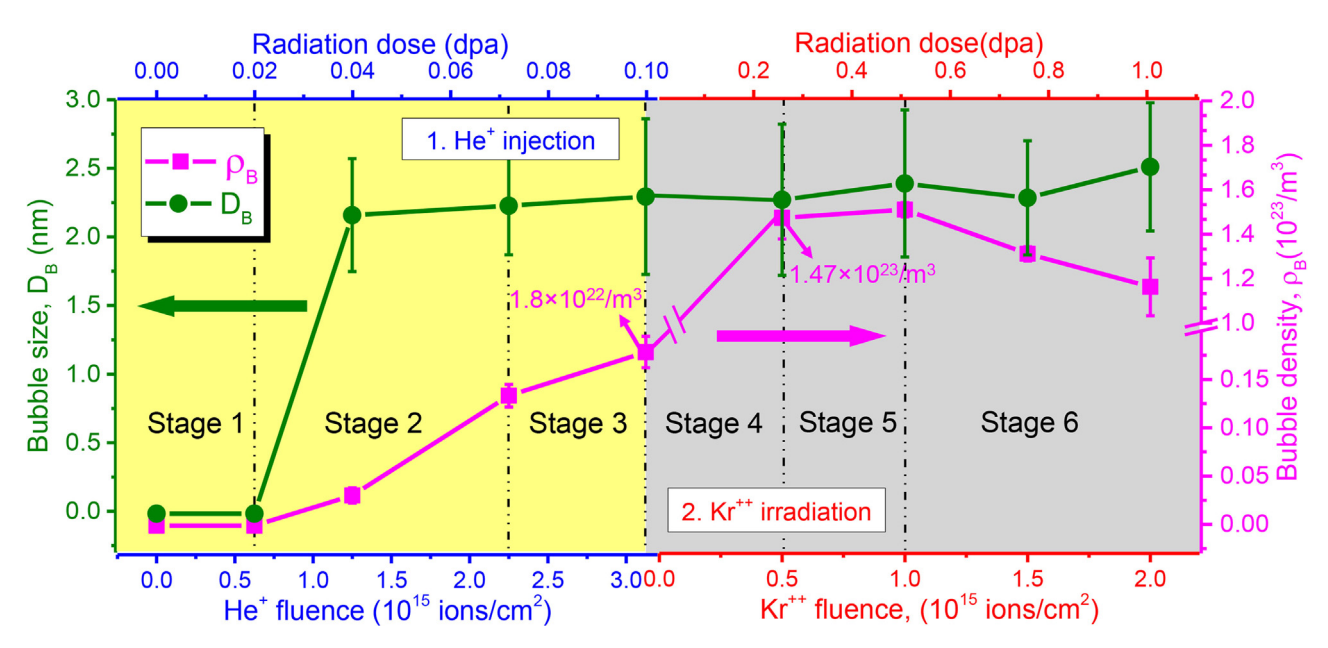


Fig. 5. Evolutions of bubble size D_B (diameter) and density $ρ_B$ under dual-beam irradiation. The entire process is divided into 6 different stages according to the variations of $ρ_B$ and D_B . Stage 1: incubation period. Stage 2: nucleation and growth. Stage 3: size maximization. Stage 4: density increment. Stage 5: density saturation. Stage 6: coarsening.

is evident that the slopes for individual void shrinkage curves are exponentially decreasing for single-beam irradiation (blue curves) but gradually leveling off for dual-beam case (red curves), indicating the void shrinkage behavior is strongly dependent on He and void size. The corresponding average growth rate $\Delta R/\Delta t$ (nm/s) is plotted as function of void radius R in Fig. 6(b). The variations of void shrinkage rate on radius can be simplified into 3 scenarios: ① when R > 5 nm, $\Delta R/\Delta t$ decreases with decreasing R for both irradiations; ② when R < 5 nm, $\Delta R/\Delta t$ drops dramatically with decreasing R for single-beam irradiation, ③ while $\Delta R/\Delta t$ increases and approaches zero (no shrinkage) at $R \approx 3$ nm for dual-beam irradiation.

3.5. Post-irradiation analysis

After irradiation, the single-beam irradiated TEM specimen remained intact when cooling to room temperature from 350 °C, so it could be carefully reexamined to identify the irradiation-induced defect clusters. Its bright-field [110] down-zone TEM micrograph in Fig. 7(a) clearly reveals numerous triangular defects with two remaining spherical voids. The triangular features are identified as stacking fault tetrahedrons (SFTs) by the HRTEM image in Fig. 7(b), as they all exhibit a peculiar V-shaped open triangle consisting of two {111} planes and are in good agreement with previous observations [44]. The SFTs range from 1 to 7 nm in edge length L_{SFT} ,

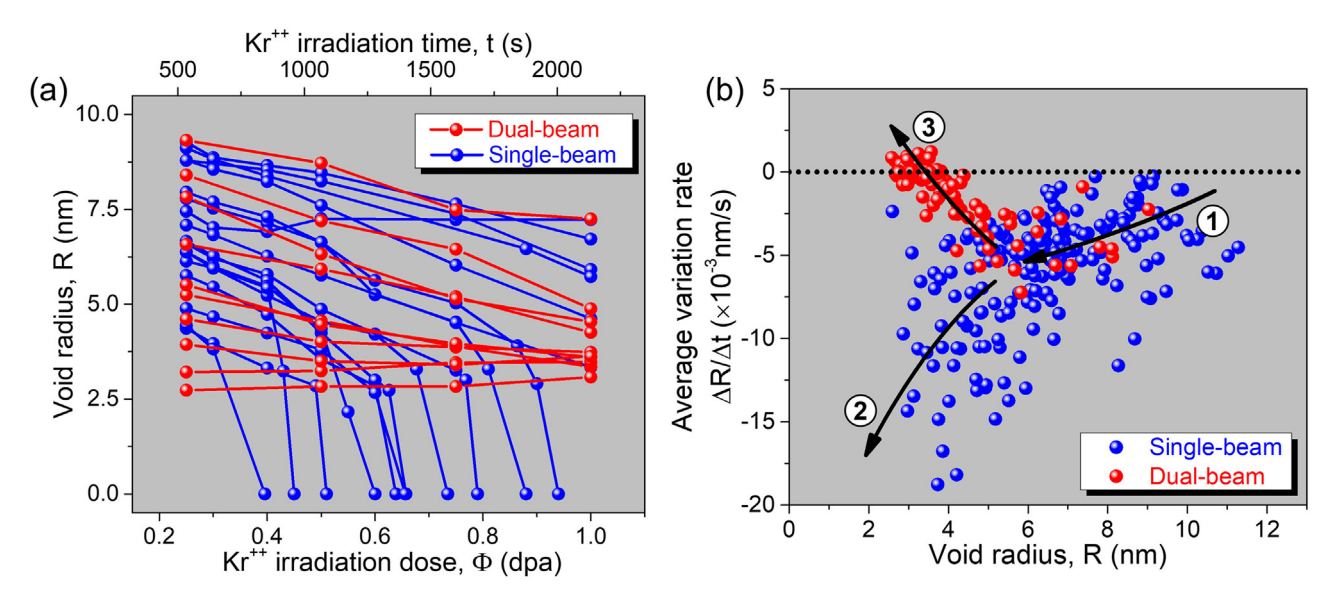


Fig. 6. Evolution of void size under dual- and single-beam irradiation over 0.25 to 1.00 dpa. (a) Void radius R versus radiation dose and time. (b) The average void size variation rate $\Delta R/\Delta t$ (nm/s) plotted as a function of R.

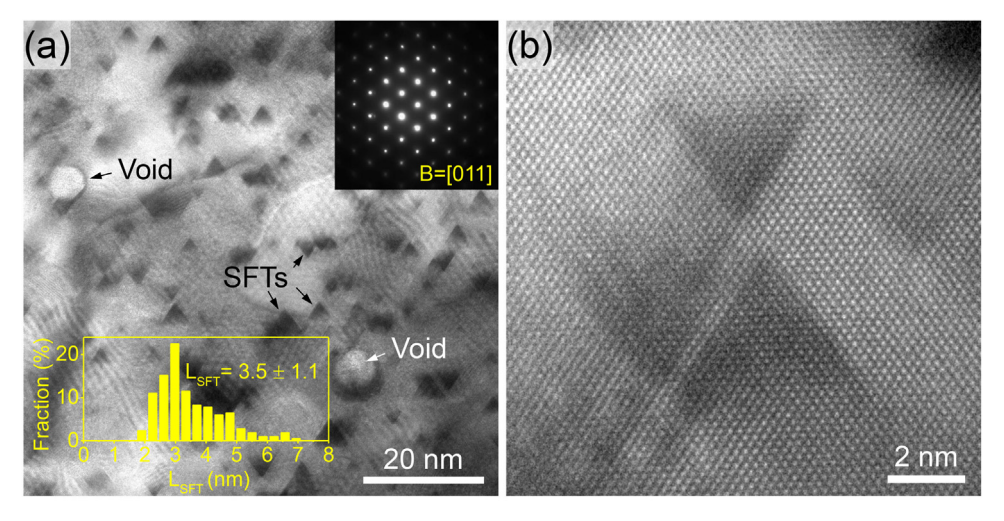


Fig. 7. Post-irradiation analysis of single-beam irradiated Cu (110). (a) Bright-field TEM micrograph showing two remaining voids surrounded by numerous SFTs. (b) HRTEM image of triangular SFTs. The inset plot in (a) shows the size distribution of SFT edge length, L_{SFT}.

as shown by the inset in Fig. 7(a). The dual-beam irradiated TEM specimen, on the other hand, embrittled to pieces after unloading from IVEM. This embrittlement could be caused by the formation of high-density He bubbles [45]. Furthermore, it is assumed that the irradiation-induced vacancy clusters in Cu would exist in the form of bubbles, rather than SFTs, when sufficient He exists [2], because He can enhance the stability of bubbles due to its high binding energy with vacancies [46].

4. Discussion

In conventional studies, cavity is a genetic term for describing the 3D vacancy (V) defect clusters with various geometric configurations depending on material properties and the nature of defect clusters [9]. Before our discussion, it is necessary to clarify different vacancy clusters. In the presence of He, they can be subdivided into three types [47]: (1) He-V clusters that are at atomic scale with a very high He/V ratio, (2) bubbles that are typically several nanometers in diameter with approximately equal numbers of Vs and He atoms, and (3) voids that are usually larger than a few ten nanometers filled with pure vacancies or a small

amount of He atoms. According to our *in situ* TEM observations in Sections 3.1-3.4, these three types of cavities behave distinctly and only the bubbles can remain stable against high-temperature ion irradiation. In contrast, most of the He-V clusters in Fig. 2 might be too tiny to be detected by TEM, but they tend to grow rapidly and evolve into stable bubbles as shown in Fig. 3(e)-(h). The voids in Fig. 3, however, tend to shrink and finally either disappear under single-beam irradiation in Fig. 3(a)-(d), or develop into stable bubbles under dual-beam irradiation in Fig. 3(e)-(h). The formation and growth of atomic He-V clusters are beyond the capability of our experiments due to the TEM resolution limit, and the reader can find some relevant atomistic simulation studies elsewhere [48–50].

In the following sections, we will begin with the introduction of a common theoretical framework for describing the kinetics of cavity growth. After that, our attention will be paid to the evolutions of voids and bubbles and the correlation between theoretical predictions and our *in situ* experimental data points. In the end, two proposed bubble coarsening models, migration and coalescence and Ostwald ripening, will be briefly discussed based on our experimental observations and theoretical calculations.

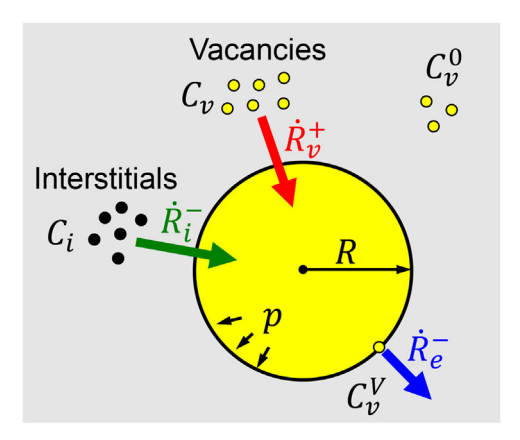


Fig. 8. Interactions between point defects and a spherical void (or bubble) with its radius R and internal pressure of p. C_i and C_v : the interstitial and vacancy concentrations in the matrix; C_v^V : the vacancy concentration at void surface; C_v^0 : thermal equilibrium vacancy concertation; \dot{R}_v^+ and \dot{R}_i^- : the variation rates due to the fluxes of vacancies and interstitials into the void, respectively; \dot{R}_e^- : the shrinkage rate due to the thermal emission of vacancies from the void surface.

4.1. Kinetics of cavity growth

The growth (or shrinkage) of a cavity in irradiated materials is determined by its interaction with radiation-induced defects. Assume a spherical void (or bubble), with a radius of R, that shrinks/grows via absorbing vacancies/interstitials from the matrix, and concurrently via emitting vacancies from its surface, as schematically illustrated in Fig. 8. Its shrinkage (\hat{R}_i^-) and growth (\hat{R}_{ν}^+) rates due to the absorption of interstitials/vacancies are given respectively by [51]:

$$\dot{R}_i^- = -\frac{D_i C_i}{R} \tag{1}$$

$$\dot{R}_{\nu}^{+} = \frac{D_{\nu}C_{\nu}}{R} \tag{2}$$

where $C_{i/v}$ is the interstitial/vacancy concentration (atomic fraction) arising from the radiation damage in the matrix, and $D_{i/v}$ is the interstitial/vacancy diffusion coefficient. In addition, its shrinkage rate (\dot{R}_{P}^{-}) due to thermal vacancy emission is given by:

$$\dot{R}_e^- = -\frac{D_v C_v^V}{R} \tag{3}$$

where C_{ν}^{V} is the vacancy concentration at void surface, as schematically shown in Fig. 8. The net void growth rate \dot{R} , therefore, is the sum of three terms above and in the form of:

$$R = R_{\nu}^{+} + R_{i}^{-} + R_{e}^{-} \tag{4}$$

At a given temperature T, the interstitial/vacancy diffusion coefficient $D_{i/\nu}$ for face-centered cubic (FCC) metals can be estimated by [51]:

$$D_{i/\nu} = \alpha a^2 \nu \exp\left(\frac{S_m^{i/\nu}}{k}\right) \exp\left(\frac{-E_m^{i/\nu}}{kT}\right)$$
 (5)

where α is a constant, 1/2 for D_i and 1 for D_v ; a is the lattice constant, 0.3615 nm for Cu; $S_m^{i/v}$ is the interstitial/vacancy migration entropy that can be neglected, and $E_m^{i/v}$ is the interstitial/vacancy migration energy, 0.12/0.8 eV for Cu; v is the Debye frequency ($\sim 10^{13} \text{ s}^{-1}$) and k is the Boltzmann's constant. Moreover, the vacancy concentration at void surface, C_v^V in Eq. (3), is related to the void radius R and internal pressure p, given by:

$$C_{v}^{V} = C_{v}^{0} \exp \left[-\frac{\Omega}{kT} \left(p - \frac{2\gamma}{R} \right) \right]$$
 (6)

where Ω is the atomic volume, 1.18 \times 10⁻²⁹ m⁻³ for Cu, and γ is the surface energy, 1.71 J/m² for Cu at 350 °C [52]. The thermal equilibrium concentration of vacancies, the term C_{ν}^{0} in Eq. (6), can be described by:

$$C_{\nu}^{0} = \exp\left(\frac{S_{f}^{\nu}}{k}\right) \exp\left(\frac{-E_{f}^{\nu}}{kT}\right) \tag{7}$$

where S_f^v is the vacancy formation entropy, 2.4k for Cu, and E_f^v is the vacancy formation energy, \sim 1.27 eV for Cu.

Eqs. (1-7) reveal that the solution to \dot{R} depends on the calculation of point defect concentration $C_{i/\nu}$. Given a certain irradiation system, its instant $C_{i/\nu}$ is determined by a series of complicated processes, including defect production, diffusion, recombination, and interactions with defect sinks; the local change of $C_{i/\nu}$ can be mathematically described by the point defect balance equations (PDBEs) [53,54]. Unfortunately, the PDBEs are nonlinear differential equations, so it is usually difficult to get their analytical solutions. To address this issue, we follow the critical bubble model (CBM) developed by Stoller et.al [55,56], and define a dimensionless parameter S_{ν}^E that is written in terms of $C_{i/\nu}$ as:

$$S_{\nu}^{E} = \frac{D_{\nu}C_{\nu} - D_{i}C_{i}}{D_{\nu}C_{\nu}^{0}} \tag{8}$$

The S_{ν}^{E} in Eq. (8) is also known as the effective vacancy supersaturation [19]. For a non-irradiation system at thermally equilibrium state, $C_{\nu} = C_{\nu}^{0}$ and C_{i} can be neglected, so $S_{\nu}^{E} = 1$; for an irradiation system, S_{ν}^{E} could be >> 1 when it is vacancy-rich, or << 1 when it is interstitial-rich.

Using Eq. (8) and substituting Eqs. (5)-(7) into Eq. (4) yield:

$$\dot{R} = \frac{D_{\nu}C_{\nu}^{0}}{R}S_{\nu}^{E} - \frac{D_{\nu}C_{\nu}^{0}}{R}\exp\left[-\frac{\Omega}{kT}\left(p - \frac{2\gamma}{R}\right)\right]$$
(9)

Eq. (9) indicates that, the growth rate of an individual void R is readily calculated if S_{ν}^{E} and p are known. In the following sections, the void growth rate will be calculated at a high dose, > 0.25 dpa, when defects are saturated and the irradiated material reaches a steady state [57].

4.2. Void shrinkage under single-beam irradiation

In the case of the single-beam heavy ion irradiation by 1 MeV Kr⁺⁺, p=0, the \dot{R} in Eq. (9) is thus simplified to be a function of the single parameter S_{ν}^{E} . The variations of \dot{R} over $S_{\nu}^{E}=-200$ to 100 are plotted in Fig. 9(a). The calculations reveal that the void nucleation and growth ($\dot{R}>0$) can be triggered only when $S_{\nu}^{E}>1$. Setting $\dot{R}=0$ (p=0) in Eq. (9) gives the critical size R_{c} for a void embryo that can evolve into a stable void, in the form of:

$$R_{c} = \frac{2\Omega\gamma}{kT \ln S_{v}^{E}} \tag{10}$$

On the other hand, if $S_{\nu}^{E} < 1$, $\dot{R} < 0$, it indicates the shrinkage of preexisting voids, which is consistent with our *in situ* observations demonstrated in Fig. 3(a)-(d). As shown in Fig. 9(b), when S_{ν}^{E} is set in a range of -300 to 1, the measured data points for void shrinkage under single-beam irradiation can be well described by the proposed CBM model presented in Section 4.1.

The fitting results in Fig. 9(b) suggest that the single-beam irradiation provides more interstitials than vacancies, which suppresses void nucleation and promotes void shrinkage rather than growth. The underlying mechanisms can be rationalized by two factors. First, the interstitial diffusion coefficient D_i is higher than the vacancy diffusion coefficient D_v , because interstitial has a lower migration energy E_m^i , as demonstrated by Eq. (5). Second, although irradiation creates equal numbers of interstitials and vacancies, the fraction of clustered vacancies is higher than that of interstitials. As

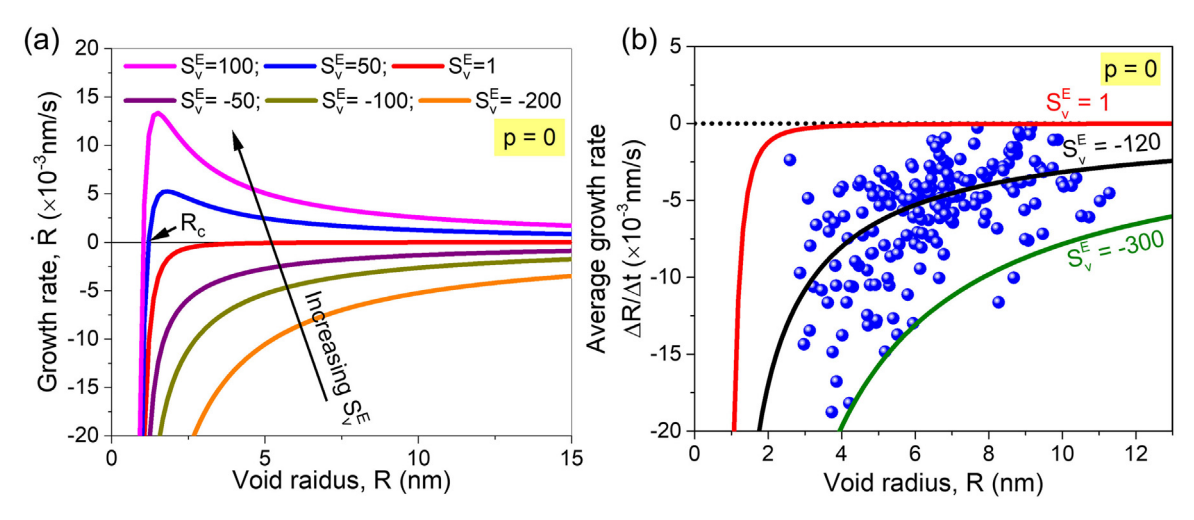


Fig. 9. Void shrinkage under single-beam irradiation by 1 MeV Kr⁺⁺ (p=0). (a) Predictions of void growth rate with increasing S_V^E from -200 to 100, plotted as a function of void radius R. Void nucleation and growth can occur when $S_V^E > 1$ and $R > R_c$. (b) The predictions fit well with experimental data points when S_V^E ranges from -300 to 1.

demonstrated in Fig. 7, a large fraction of the irradiation-induced vacancies would aggregate into immobile SFTs, a special 3D vacancy cluster widely observed in FCC metals with medium-to-low stacking fault energies [58,59]. One SFT is composed of 6 immobile 1/6 <110> stair-rod dislocations and 4 intrinsic {111} stacking faults [60,61]. The stable dislocation structure of SFTs makes it difficult for them to interact with other point defects [62,63]. In contrast, the preexisting nanovoids can easily absorb a net number of interstitials, resulting in void shrinkage as shown in Fig. 3(a)-(d). Consequently, the system appears to be 'interstitial-rich' with S_{ν}^{E} < 1, and the preexisting voids progressively shrink with increasing dose. We speculate that radiation-induced void swelling might occur if there are high-density interstitial-biased sinks, such as dislocations [64].

4.3. Foil surface effect on void shrinkage

Although a majority of the voids tend to shrink prominently under 1 MeV Kr⁺⁺ irradiation, some of them reduce slightly in size, such as the survivals A-F in Fig. 3(a)-(d). Moreover, the void shrinkage rate varies from one to another, and the S_{ν}^{E} in Fig. 9(b) falls in a broad range between -300 and 1. Similar void shrinkage behavior has also been reported by the in situ TEM annealing study on the irradiation-induced voids in Al [65]. The fact that voids shrink over a wide range of rates may arise from their different distances to the TEM foil surface. It has been pointed out that the near-surface voids shall shrink faster by yielding their vacancies to free surface [65], and significant void swelling suppression have been observed at depths within \sim 400 nm from the surface in ion irradiation studies [34]. Such assumption also agrees with our TEM observation presented in Supplementary Fig. S3; the void porosity decreases with decreasing film thickness, indicating that the foil surface can facilitate void shrinkage at thinner areas.

4.4. Bubble nucleation and void shrinkage under dual-beam irradiation

According to our *in situ* dual-beam irradiation observations, He can affect cavity evolution generally in two aspects: (1) promoting bubble nucleation, and (2) retarding void shrinkage. A quantitative computation of their growth rate \dot{R} in Eq. (9) requires the evaluation of the magnitude of internal pressure p, apart from the effective vacancy supersaturation S_{ν}^{E} . Assume a cavity at the thermodynamically equilibrium state has its internal pressure p balanced by

its surface tension γ , then the corresponding equilibrium pressure p_0 is given by the well-known capillarity equation [66]:

$$p_0 = \frac{2\gamma}{P} \tag{11}$$

Using Eq. (11) and taking a typical value of R=1 nm for the small He bubbles in Cu at 350 °C, we arrive at an equilibrium pressure p_0 of 3.42 GPa. This estimation suggests that the real pressure within nanometer sized He bubbles is extremely high. Unfortunately, an accurate equation of state for such small high-pressure bubbles is still lacking [66,67]. So far, some proposed equations of state include the simple models of ideal gas, van der Waals, and hard sphere [67], as well as empirical relations based on experimental results [68]. Note that all these models have their advantages and limitations. Whether they are valid or not depends on cavity pressure, temperature, and volume. Here, for simplicity, we consider a modified ideal gas model to describe the bubbles or voids under dual-beam irradiation, which shows:

$$p = \frac{3n_{He}kT}{4\pi R^3} \kappa \tag{12}$$

where κ is defined as the real gas compressibility factor, a ratio of the real pressure to the ideal gas pressure, and $\kappa=1$ applies for ideal gas [67]. In addition, n_{He} is the number of He atoms inside cavity, and it can be estimated using the He/V ratio ν :

$$n_{He} = \frac{4\pi R^3}{3\Omega} \nu \tag{13}$$

It has been pointed out that after He atoms are trapped by a cavity in metals they can barely escape [47]. As such, the cavity pressure p increases with increasing ν until it approaches a maximum value $p_{\rm max}$ beyond which the internal pressure may be released via dislocation loop punching [69]. In FCC meals, the punched dislocation loop can be assumed as a prismatic Frank loop. Setting its Burgers vector magnitude as b (\sim 2.1 nm for Cu) gives [47]:

$$p_{\text{max}} = \frac{2\gamma}{R} + \frac{\mu b}{R} \tag{14}$$

where μ is the shear modulus, ~48.3 GPa for Cu [68].

Using the empirical equation of state established by Mills et al [70], Donnelly estimated the He/V ratios under p_0 and $p_{\rm max}$ of the spherical bubbles in Cu at room temperature [68]. His estimations are listed in Table 1, together with the corresponding He atom numbers n_{He} calculated using Eq. (13). As shown in Fig. 5 and 6, the stable He bubbles in our dual-beam irradiation study at 350 °C

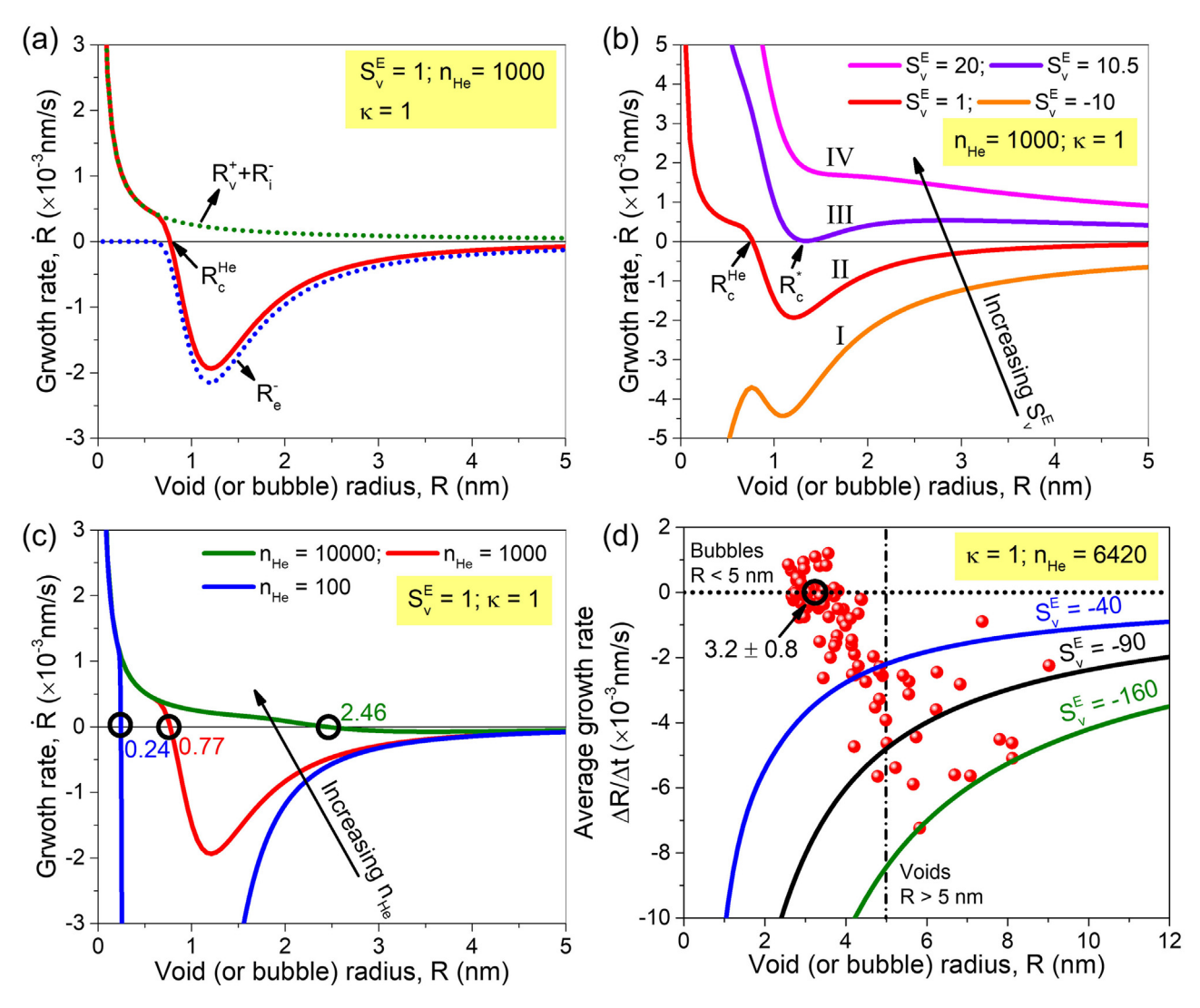


Fig. 10. Bubble nucleation and void shrinkage under dual-beam irradiation. (a) The net growth rate (red curve) of a void (or bubble) resulting from defect absorption (dotted green curve) and vacancy emission (dotted blue curve). R_v^{Ele} refers to the predicted stable size in the presence of He. (b) Predictions of growth rate with increasing S_v^{Ele} from -10 to 20. (c) Predictions of growth rate with increasing n_{He} from 100 to 10000. (d) Correlation between experimentally measured void shrinkage rates (red data points) and CBM predictions (solid curves). The predictions fit well with experimental data points only when R > 5 nm and S_v^{Ele} ranges from -160 to -40.

Table 1 Estimations of equilibrium and maximum pressures, He/V ratios, and He atom numbers for small bubbles in Cu (after [68]). p_0 : equilibrium pressure; p_{max} : maximum pressure; ν : He/V ratio; n_{He} : the number of He atoms.

Cavity radius R (nm)	Equilibrium state [Eq. (11)]			Maximum state [Eq. (14)]		
	p_0 (GPa)	v	n _{He}	p _{max} (GPa)	ν	n _{He}
1	2.8	1.02	362	13.6	1.71	607
2	1.4	0.80	2271	6.8	1.37	3889
3	0.9	0.67	6420	4.5	1.20	11496

also range from 1 to 3 nm in radius. However, due to high temperature effect, the equilibrium He atom numbers in Table 1 should be overestimated compared with our case.

To reveal the influence of He on cavity evolution, we first consider an ideal gas system ($\kappa=1$) under non-irradiation state ($S_{\nu}^{E}=1$). Setting n_{He} as 1000 and substituting Eq. (12) into Eq. (9) yield the variation of cavity growth rate as a function of cavity radius, as shown by the red solid line in Fig. 10(a). The total growth rate in Fig. 10(a) results from two contributions: $\dot{R}_{\nu}^{+}+\dot{R}_{i}^{-}$ the net point defect diffusion from the matrix, and \dot{R}_{e}^{-} the vacancy

thermal emission of cavity itself; they are also plotted in green and blue dotted lines, respectively, in Fig. 10(a). As \dot{R}_e^- always leads to cavity shrinkage, the cavity can only grow or remain stable when it receives more vacancies than interstitials from the matrix. In other words, S_c^E must be positive for cavity nucleation and growth. When S_c^E decreases, the cavity can reach a stable state if $\dot{R}_v^+ + \dot{R}_i^- = \dot{R}_e^-$. In this case, the growth rate curve intersects with $\dot{R}=0$ at a critical value, as denoted by the R_c^{He} in Fig. 10(a). Note that unlike the unstable critical size R_c defined in Eq. (9), R_c^{He} refers to a stable critical size, since the cavity will grow $(\dot{R}>0)$ if $R< R_c^{He}$, or it will shrink $(\dot{R}<0)$ if $R>R_c^{He}$. In addition, Eq. (9) also indicates that He can decrease vacancy emission rate \dot{R}_e^- by increasing internal pressure p, which might stabilize voids by reducing their shrinkage rate.

For a cavity with a fixed amount of He atoms, whether it can evolve into a stable bubble at R_c^{He} depends on the variation of S_{ν}^E . Mathematically, there could be four cases, as illustrated by the four typical curves plotted in Fig. 10(b). In case I, $S_{\nu}^E = -10$ and all the small cavities have a negative growth rate \dot{R} , so they will shrink continually and be dissolved in the matrix. In reality, however, small gas-filled cavities, such as He bubbles, cannot eventu-

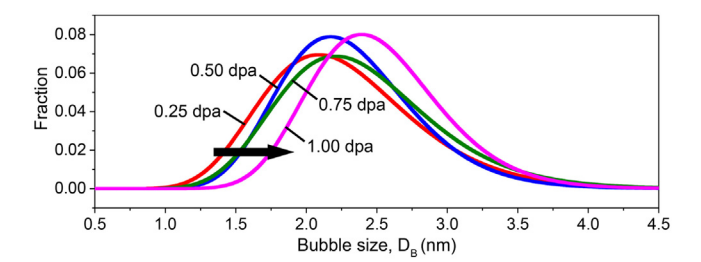


Fig. 11. Bubble size distributions at various doses. Each distribution curve is fitted from 500 raw data points (see Supplementary Fig. S4). The arrow marks a slight shift rightward with increasing dose, indicative of bubble coarsening.

ally disappear because there is a minimum volume occupied by gas atoms [51]. The case I merely applies for large cavities that prefer shrinkage to swelling. The case II is in qualitative agreement with our observations in Section 3 where He bubbles can remain stable at a critical size R_c^{He} , as illustrated in Fig. 3. With increasing S_c^F , the stable bubbles will finally turn into unstable voids that tend to grow without limit, as demonstrated by case IV. The transition state from bubble to void is presented by case III in Fig. 10(b). In this case, there is a critical radius R_c^* that corresponds to the maximum value of stable bubbles.

Fig. 10(c) demonstrates the variations of \dot{R} with $S_{\nu}^{E}=1$. It shows that R_{c}^{He} increases from 0.24 to 2.46 nm when n_{He} increases from 100 to 1000. This can account for our *in situ* observations in Fig. 3(e-h) where the bubbles evolving from preexisting voids are larger than those evolving from invisible He-V clusters, because the former ones contain more He atoms.

Eventually, the correlation between measured data points (red balls) and theoretical predictions (solid curves) are plotted in Fig. 10(d). The plot can be roughly divided into two regions bounded by the vertical dashed line. When R > 5 nm, the cavities are voids in nature, and their measured growth rates fit well with the calculated curves obtained from Eqs. (9) and (12) by setting $\kappa = 1$, $n_{He} = 6420$ (see Table 1), and S_{ν}^{E} between -160 and -40. As described by Eq. (8), S_v^E indicates the vacancy supersaturation relative to interstitials. Compared with single-beam irradiation, the S_{ν}^{E} is higher in dual-beam irradiation, because some of the irradiation-induced vacancies in the former case cluster into SFTs that are immobile and barely interact with preexisting voids or irradiation-induced interstitials. In contrast, the irradiation-induced vacancies in the latter case form bubbles that can act as effective defect sinks and absorb interstitials and vacancies, thus reducing the interstitials diffusing into voids, that is, increasing the value of S_{ν}^{E} in Fig. 10(d). When R < 5, the cavities transmit progressively from voids to bubbles, so the predictions of growth rate using ideal gas model ($\kappa = 1$) are no longer appropriate. According to a recent molecular dynamic simulation study by Stoller and Osetsky [67], the real gas compressibility factor κ in Eq. (11) increases exponentially when R deceases to 1-3 nm for the small He bubbles in Fe. Therefore, more accurate calculations regarding the kinetics of bubble growth may require further theoretical or simulation stud-

4.5. Bubble coarsening models: Ostwald ripening vs. migration and coalescence

In the preceding sections, we discussed the void shrinkage under single- and dual-beam irradiations. This section is mainly concerned with the size change of He bubbles. As shown in Fig. 3(e-h) and Fig. 5, the density of bubbles decreases while their average size increases during 1 MeV Kr⁺⁺ irradiation. The corresponding bubble size distributions are shown in Fig. 11. It has been found

that the distribution curves shift rightward with increasing dose as the bubbles are subject to coarsening. However, identifying the coarsening mechanism is experimentally difficult due to the sample tilting and shifting as well as resolution limit. Previous studies have demonstrated that the bubble coarsening is of great complexity, influenced by factors like stress, microstructure, and temperature [71,72]. To describe the coarsening process, several models have been proposed; especially, there are two typical models that have been the most frequently discussed and compared, including the Ostwald ripening (OR) and the migration and coalescence [73-76]. On the one hand, OR involves the resolution and reabsorption of He atoms or vacancies, driven by the concentration gradient between the surfaces of small and large cavities [77]. According to OR model, large cavities are expected to grow by consuming smaller ones. In the current study, however, we did not find the void growth at the expense of small bubbles, but instead we observed the void shrinkage, as shown in Fig. 3(e-h). Moreover, our theoretical calculations suggested that bubbles are unlikely to grow through OR, as He is hardly re-dissolved after combing with vacancies and being trapped inside bubbles. As for MC, on the other hand, it is assumed to be driven by temperature gradient and occurs by surface diffusion [42]. Phase-field simulation studies demonstrated that voids may migrate one-dimensionally and up the temperature gradient [78]. According to our recent in situ TEM irradiation study, however, small voids ($<6.5 \pm 1.5$ nm) can move randomly and rapidly (>0.1nm/s) when irradiated by a single beam of 1 MeV Kr⁺⁺ at 350 °C without a temperature gradient, presumably resulting from their direct interactions with radiation damage cascades [37]. Considering the smaller size of bubbles (only 1-3 nm in diameter), if they could migrate like voids, they would move much faster and be readily absorbed by TEM foil surface. However, most of such tiny bubbles were preserved after a long time (\sim 2100 s) of 1 MeV Kr⁺⁺ irradiation (see Fig. 5). The bubbles appear to be 'frozen' by high density He, as the diffusion at bubble internal surface is suppressed by high internal pressure [79]. Despite the frozen effect, it is still possible for bubbles to migrate and coalescence in the presence of radiation damage cascades, as evidenced by Fig. 4(c-d). Moreover, the frozen effect could be an important reason for the stability of bubbles. To obtain a better understanding of bubble migration will require further simulation studies on the effects caused by internal pressure.

5. Conclusions

Comparative studies of in situ TEM ion irradiation have been conducted between single- and dual-beam irradiated single-crystal Cu (110) with preexisting nanovoids. The results revealed that implanted He plays an important role in the bubble nucleation and void shrinkage under heavy ion irradiation environment. Most of the preexisting voids shrank continuously and finally disappeared when irradiated by a single 1 MeV Kr++. The shrinkage mechanism can be attributed to the net flux of interstitials into voids. When pre-injected by 14 keV He+, the voids stopped shrinking and remained stable when their diameter reduced to ~3 nm, albeit continuous irradiation by 1MeV Kr++. The evolution of bubbles under dual-beam irradiation can be divided into several distinct stages, including incubation period, nucleation and growth, size saturation, density increment, and saturation, and coarsening. Post-irradiation analyses revealed that the remaining defect clusters are dominated by SFTs in single-beam irradiated specimen but primarily in the form of bubbles in dual-beam irradiated specimen. The kinetics of void shrinkage for single-beam irradiation can be well described by proposed critical bubble model when internal pressure equals 0 and there is an enrichment of interstitials.

Declaration of Competing Interest

The authors declare that they have no known competing financial interests or personal relationships that could have appeared to influence the work reported in this paper.

Acknowledgements

We acknowledge the financial support by NSF-CMMI-1728419. Zhongxia Shang and Haiyan Wang acknowledge the support from the U.S. Office of Navel Research(N00014-22-1-2160 and N00014-20-1-2043). Zhongxia Shang is also supported by NSF-DMR-Metallic Materials and Nanostructures Program under grant 1611380. IVEM at Argonne National Laboratory is supported by DOE, Office of Nuclear Energy. We also acknowledge access to Microscopy center at School of Materials Engineering at Purdue University.

Supplementary materials

Supplementary material associated with this article can be found, in the online version, at doi:10.1016/j.actamat.2022.118293.

References

- [1] L.K. Mansur, Void swelling in metals and alloys under irradiation: an assessment of the theory, Nucl. Technol. 40 (1) (1978) 5–34.
- [2] S. Zinkle, W. Wolfer, G. Kulcinski, L. Seitzman II, Effect of oxygen and helium on void formation in metals, Philos. Mag. A 55 (1) (1987) 127–140.
- [3] J. Knaster, A. Moeslang, T. Muroga, Materials research for fusion, Nat. Phys. 12 (5) (2016) 424–434.
- [4] I. Cook, Materials research for fusion energy, Nat. Mater. 5 (2) (2006) 77.
- [5] K. Farrell, M. Lewis, N. Packan, Simultaneous bombardment with helium, hydrogen, and heavy ions to simulate microstructural damage from fission or fusion neutrons.[4 MeV/sup 58/Ni beam], Scr. Metall.;(United States) 12 (12) (1978).
- [6] K. Farrell, Experimental effects of helium on cavity formation during irradiation—a review, Radiat. Eff. 53 (3-4) (1980) 175–194.
- [7] Y. Dai, G. Odette, T. Yamamoto, in: 1.06-The Effects of Helium in Irradiated Structural Alloys, Comprehensive nuclear materials, Elsevier Oxford, 2012, pp. 141–193.
- [8] C. Fan, C. Li, C.M. Parish, Y. Katoh, X. Hu, Helium effects on the surface and subsurface evolutions in single-crystalline tungsten, Acta Mater. 203 (2021) 116420
- [9] S. Zinkle, 1.03-Radiation-Induced effects on microstructure, Compreh. Nucl. Mater. 1 (2012) 65–98.
- [10] R.E. Stoller, The influence of helium on microstructural evolution: Implications for DT fusion reactors, J. Nucl. Mater. 174 (2-3) (1990) 289–310.
- [11] K. Farrell, P. Maziasz, E. Lee, L. Mansur, Modification of radiation damage microstructure by helium, Radiat. Eff. 78 (1-4) (1983) 277–295.
- [12] J. Kai, G. Kulcinski, 14 MeV nickel-ion irradiated HT-9 ferritic steel with and without helium pre-implantation, J. Nucl. Mater. 175 (3) (1990) 227–236.
- [13] L. Wang, S. Zinkle, R. Dodd, G. Kulcinski, Effects of preinjected helium in heavy-ion irradiated nickel and nickel-copper alloys, Metall. Trans. A 21 (7) (1990) 1847–1851.
- [14] X. Wang, A.M. Monterrosa, F. Zhang, H. Huang, Q. Yan, Z. Jiao, G.S. Was, L. Wang, Void swelling in high dose ion-irradiated reduced activation ferritic-martensitic steels, J. Nucl. Mater. 462 (2015) 119–125.
- [15] A. Bhattacharya, E. Meslin, J. Henry, B. Décamps, A. Barbu, Dramatic reduction of void swelling by helium in ion-irradiated high purity α -iron, Mater. Res. Lett. 6 (7) (2018) 372–377.
- [16] A.M. Monterrosa, Z. Jiao, G.S. Was, The influence of helium on cavity evolution in ion-irradiated T91, J. Nucl. Mater. 509 (2018) 707–721.
- [17] L. Mansur, W. Coghlan, Mechanisms of helium interaction with radiation effects in metals and alloys: A review, J. Nucl. Mater. 119 (1) (1983) 1–25.
- [18] E. Getto, Z. Jiao, A. Monterrosa, K. Sun, G. Was, Effect of pre-implanted helium on void swelling evolution in self-ion irradiated HT9, J. Nucl. Mater. 462 (2015) 458–469.
- [19] Y. Dai, G. Odette, T. Yamamoto, 06-The effects of helium in irradiated structural alloys. Comprehens. Nucl. Mater. 1 (2012) 141–193.
- [20] B. Kaiser, C. Dethloff, E. Gaganidze, D. Brimbal, M. Payet, P. Trocellier, L. Beck, J. Aktaa, TEM study and modeling of bubble formation in dual-beam He+/Fe3+ ion irradiated EUROFER97, J. Nucl. Mater. 484 (2017) 59–67.
- [21] N. Packan, K. Farrell, Simulation of first wall damage: effects of the method of gas implantation, J. Nucl. Mater. 85 (1979) 677–681.
- [22] L. Jiang, Q. Peng, P. Xiu, Y. Yan, Z. Jiao, C. Lu, T. Liu, C. Ye, R. Shu, Y. Liao, Elucidating He-H assisted cavity evolution in alpha Cr under multiple ion beam irradiation, Scr. Mater. 187 (2020) 291–295.

[23] K. Hattar, D.C. Bufford, D.L. Buller, Concurrent in situ ion irradiation transmission electron microscope, Nucl. Instrum. Methods Phys. Res. Sect. B 338 (2014) 56–65

- [24] M. Li, M. Kirk, P. Baldo, D. Xu, B. Wirth, Study of defect evolution by TEM with in situ ion irradiation and coordinated modeling, Philos. Mag. 92 (16) (2012) 2048–2078.
- [25] K. Yu, C. Fan, Y. Chen, J. Li, X. Zhang, Recent studies on the microstructural response of nanotwinned metals to in situ heavy ion irradiation, JOM 72 (1) (2020) 160–169.
- [26] G. Was, Z. Jiao, E. Getto, K. Sun, A. Monterrosa, S. Maloy, O. Anderoglu, B. Sencer, M. Hackett, Emulation of reactor irradiation damage using ion beams, Scr. Mater. 88 (2014) 33–36.
- [27] D. Xu, B.D. Wirth, M. Li, M.A. Kirk, Combining in situ transmission electron microscopy irradiation experiments with cluster dynamics modeling to study nanoscale defect agglomeration in structural metals, Acta Mater. 60 (10) (2012) 4286–4302.
- [28] M.A. Kirk, M. Li, D. Xu, B.D. Wirth, Predicting neutron damage using TEM with in situ ion irradiation and computer modeling, J. Nucl. Mater. 498 (2018) 199–212.
- [29] D. Brimbal, B. Décamps, A. Barbu, E. Meslin, J. Henry, Dual-beam irradiation of α -iron: heterogeneous bubble formation on dislocation loops, J. Nucl. Mater. 418 (1-3) (2011) 313–315.
- [30] I. Ipatova, R. Harrison, S. Donnelly, M. Rushton, S. Middleburgh, E. Jimenez-Metere, Void evolution in tungsten and tungsten-5wt,% tantalum under in-situ proton irradiation at 800 and 1000°C, J. Nucl. Mater. (2019).
- [31] G. Odette, P. Miao, D. Edwards, T. Yamamoto, R. Kurtz, H. Tanigawa, Helium transport, fate and management in nanostructured ferritic alloys: In situ helium implanter studies, J. Nucl. Mater. 417 (1-3) (2011) 1001–1004.
- [32] D. Brimbal, B. Décamps, J. Henry, E. Meslin, A. Barbu, Single-and dual-beam in situ irradiations of high-purity iron in a transmission electron microscope: Effects of heavy ion irradiation and helium injection, Acta Mater. 64 (2014) 391–401.
- [33] M. Kirk, X. Yi, M. Jenkins, Characterization of irradiation defect structures and densities by transmission electron microscopy, J. Mater. Res. 30 (9) (2015) 1195–1201.
- [34] S. Zinkle, L. Snead, Opportunities and limitations for ion beams in radiation effects studies: bridging critical gaps between charged particle and neutron irradiations, Scr. Mater. 143 (2018) 154–160.
- [35] Y. Chen, K.Y. Yu, Y. Liu, S. Shao, H. Wang, M. Kirk, J. Wang, X. Zhang, Damage-tolerant nanotwinned metals with nanovoids under radiation environments, Nat. Commun. 6 (1) (2015) 1–8.
- [36] C. Fan, Y. Chen, J. Li, J. Ding, H. Wang, X. Zhang, Defect evolution in heavy ion irradiated nanotwinned Cu with nanovoids, J. Nucl. Mater. 496 (2017) 293–300.
- [37] C. Fan, R.G.S. Annadanam, Z. Shang, J. Li, M. Li, H. Wang, A. El-Azab, X. Zhang, Irradiation induced void spheroidization, shrinkage and migration in Cu at elevated temperatures: An in situ study, Acta Mater. 201 (2020) 504–516.
- [38] C. Fan, A. Sreekar, Z. Shang, J. Li, M. Li, H. Wang, A. El-Azab, X. Zhang, Radiation induced nanovoid shrinkage in Cu at room temperature: An in situ study, Scr. Mater. 166 (2019) 112–116.
- [39] S.J. Zinkle, K. Farrell, Void swelling and defect cluster formation in reactor-irradiated copper, J. Nucl. Mater. 168 (3) (1989) 262–267.
- [40] J.F. Ziegler, Nucl. Instrum. Methods Phys. Res. Sect. B 219 (2004) 1027–1036.
- [41] D.B. Williams, C.B. Carter, in: The Transmission Electron Microscope, Transmission Electron Microscopy, Springer, 1996, pp. 3–17.
- [42] R. Barnes, D. Mazey, The migration and coalescence of inert gas bubbles in metals, in: Proceedings of the Royal Society of London. Series A. Mathematical and Physical Sciences, 275, 1963, pp. 47–57.
- [43] K. Ono, K. Arakawa, K. Hojou, Formation and migration of helium bubbles in Fe and Fe-9Cr ferritic alloy, J. Nucl. Mater. 307 (2002) 1507-1512.
- [44] W. Coene, H. Bender, S. Amelinckx, High resolution structure imaging and image simulation of stacking fault tetrahedra in ion-implanted silicon, Philos. Mag. A 52 (3) (1985) 369–381.
- [45] D. Kramer, H. Brager, C. Rhodes, A. Pard, Helium embrittlement in type 304 stainless steel, J. Nucl. Mater. 25 (2) (1968) 121–131.
- [46] W. Wilson, C. Bisson, M. Baskes, Self-trapping of helium in metals, Phys. Rev. B 24 (10) (1981) 5616.
- [47] H. Trinkaus, Energetics and formation kinetics of helium bubbles in metals, Radiat, Eff. 78 (1-4) (1983) 189-211.
- [48] C.-C. Fu, F. Willaime, Ab initio study of helium in α Fe: Dissolution, migration, and clustering with vacancies, Phys. Rev. B 72 (6) (2005) 064117.
- [49] C.S. Becquart, C. Domain, Migration energy of He in W revisited by ab initio calculations, Phys. Rev. Lett. 97 (19) (2006) 196402.
- [50] W. Wilson, M. Baskes, C. Bisson, Atomistics of helium bubble formation in a face-centered-cubic metal, Phys. Rev. B 13 (6) (1976) 2470.
- [51] G.S. Was, in: Irradiation-Induced Voids and Bubbles, Fundamentals of Radiation Materials Science, Springer, 2017, pp. 379–484.
- [52] W. Tyson, W. Miller, Surface free energies of solid metals: Estimation from liquid surface tension measurements, Surf. Sci. 62 (1) (1977) 267–276.
- [53] R. Sizmann, The effect of radiation upon diffusion in metals, J. Nucl. Mater. 69 (1978) 386–412.
- [54] G.S. Was, Fundamentals of Radiation Materials Science: Metals and Alloys, Springer, 2016.
- [55] R. Stoller, G. Odette, Analytical solutions for helium bubble and critical radius parameters using a hard sphere equation of state, J. Nucl. Mater. 131 (2-3) (1985) 118–125.

- [56] G. Odette, M. Alinger, B. Wirth, Recent developments in irradiation-resistant steels, Annu. Rev. Mater. Res. 38 (2008) 471-503.
- [57] N. Nita, R. Schaeublin, M. Victoria, Impact of irradiation on the microstructure of nanocrystalline materials, J. Nucl. Mater. 329 (2004) 953-957.
- [58] S. Zinkle, R. Sindelar, Defect microstructures in neutron-irradiated copper and stainless steel, J. Nucl. Mater. 155 (1988) 1196-1200.
- [59] R. Schäublin*, Z. Yao, N. Baluc, M. Victoria, Irradiation-induced stacking fault tetrahedra in fcc metals, Philos. Mag. 85 (4-7) (2005) 769-777.
- [60] M. Loretto, P. Phillips, M. Mills, Stacking fault tetrahedra in metals, Scr. Mater. 94 (2015) 1-4
- [61] M. Kiritani, Story of stacking fault tetrahedra, Mater. Chem. Phys. 50 (2) (1997) 133-138.
- [62] Y.N. Osetsky, A. Serra, M. Victoria, S. Golubov, V. Priego, Vacancy loops and stacking-fault tetrahedra in copper: II. Growth, shrinkage, interactions with point defects and thermal stability, Philos. Mag. A 79 (9) (1999) 2285-2311.
- [63] L. Zhang, C. Lu, G. Michal, G. Deng, K. Tieu, The formation and destruction of stacking fault tetrahedron in fcc metals: A molecular dynamics study, Scr. Mater. 136 (2017) 78-82.
- [64] W. Wolfer, The dislocation bias, J. Comput. Aided Mater. Des. 14 (3) (2007) 403-417.
- [65] N. Packan, D. Braski, Electron microscope in situ annealing study of voids induced by irradiation in aluminum, J. Nucl. Mater. 34 (3) (1970) 307-314.
- [66] A. Caro, D. Schwen, J. Hetherly, E. Martinez, The capillarity equation at the nanoscale: Gas bubbles in metals, Acta Mater. 89 (2015) 14-21.
- [67] R. Stoller, Y.N. Osetsky, An atomistic assessment of helium behavior in iron, J. Nucl. Mater. 455 (1-3) (2014) 258-262.

- [68] S. Donnelly, The density and pressure of helium in bubbles in implanted metals: a critical review, Radiat. Eff. 90 (1-2) (1985) 1-47.
- [69] J. Evans, The role of implanted gas and lateral stress in blister formation mechanisms, J. Nucl. Mater. 76 (1978) 228-234.
- R. Mills, D. Liebenberg, J. Bronson, Equation of state and melting properties of He 4 from measurements to 20 kbar, Phys. Rev. B 21 (11) (1980) 5137.

 [71] J. Gao, L. Bao, H. Huang, Y. Li, J. Zeng, Z. Liu, R. Liu, L. Shi, Evolution law of
- helium bubbles in hastelloy N alloy on post-irradiation annealing conditions, Materials 9 (10) (2016) 832.
- [72] D. Braski, H. Schroeder, H. Ullmaier, The effect of tensile stress on the growth of helium bubbles in an austenitic stainless steel, J. Nucl. Mater. 83 (2) (1979) 265-277.
- [73] P. Goodhew, On the migration of helium bubbles, Radiat. Eff. 78 (1-4) (1983) 381 - 383.
- [74] H. Trinkaus, B. Singh, Helium accumulation in metals during irradiation-where do we stand? J. Nucl. Mater. 323 (2-3) (2003) 229-242.
- H. Schroeder, P.F. Fichtner, On the coarsening mechanisms of helium bubbles-Ostwald ripening versus migration and coalescence, J. Nucl. Mater. 179 (1991) 1007-1010.
- [76] C. Jiang, J.-H. Ke, P.-C.A. Simon, W. Jiang, L.K. Aagesen Jr, Atomistic and Mesoscale Simulations to Determine Effective Diffusion Coefficient of Fission Products in SiC, Idaho National Lab.(INL), Idaho Falls, ID (United States), 2021.
- [77] J. Rothaut, H. Schroeder, H. Ullmaier, The growth of helium bubbles in stainless steel at high temperatures, Philos. Mag. A 47 (5) (1983) 781-795.
- S.Y. Hu, C. Henager Jr, Phase-field simulation of void migration in a temperature gradient, Acta Mater. 58 (9) (2010) 3230–3237. [79] N. Marochov, L. Perryman, P. Goodhew, Growth of inert gas bubbles after im-
- plantation, J. Nucl. Mater. 149 (3) (1987) 296-301.